ADVANCED ELECTRONIC MATERIALS
www.advelectronicmat.de

Rigid Exchange Coupling in Rare-Earth-Lean Amorphous Hard/Soft Nanocomposites

Parul Rani, Giuseppe Muscas, Henry Stopfel, Gabriella Andersson, and Petra Erika Jönsson**

Electrification of vehicles and renewable energy is increasing the demand for permanent magnets, but the cost and scarcity of rare-earth metals is an obstacle. Creating nanocomposites of rigidly exchange-coupled hard and soft magnets, for which the magnetization reversal occurs as in a single magnetic-phase material, is a promising route toward rare-earth-lean permanent magnets with high energy products. The hard/soft exchange coupling is, however, often reduced due to rough interfaces and structural defects, resulting in exchange-spring behavior rather than rigid exchange coupling. Here, it is shown that artificially sandwiched hard and soft amorphous magnets produced by magnetron sputtering exhibit smooth interfaces, and the first order reversal curve (FORC) technique is used to show that the hard and the soft phases are rigidly exchange coupled. Micromagnetic simulations, using a random-anisotropy model, are used to predict the thickness limit of the rigid exchange coupling. A great advantage of amorphous hard/soft composites is the possibility to obtain a wide range of magnetic properties by finely tuning the composition of the individual phases.

1. Introduction

For the past few years, a major goal within the magnetism community has been to decrease the use of rare-earth elements in strong permanent magnets.[1,2] Samarium is, at the moment, the only non-critical rare-earth metal used in permanent magnets.[3] An efficient route to decrease the use of any rare-earth element is to create hard/soft exchange-coupled magnetic materials.[1,4–6] The exchange coupling between the hard and the soft magnetic phases can, in addition, create an energy product, $(BH)_{max}$, considerably larger than for a single hard phase, since the strong coercivity H_c of the hard phase is combined with the high saturation magnetization M_s of the soft phase.[7] With sufficiently strong exchange coupling between the two magnetic phases, the soft phase moments will follow the hard phase during magnetization reversal. Such a rigidly exchange-coupled composite exhibits a magnetic hysteresis loop characteristic of a single ferromagnetic phase,[8] rather than a loop with drops, kinks, or shoulders from two superposed switching processes.[9] For most practical applications, it is also crucial that the Curie temperature T_c of the composite material is well above room temperature, and that the overall M_s value is large. A model for the interfacial exchange-spring coupling between a soft and a hard phase was introduced by Goto et al.[10] According to that model, the two phases can reverse their moments coherently, that is, as a single component, only if the coupling is strong enough to extend from the interface through the entire thickness of the soft phase. Thus, for a given combination of soft and hard materials, rigid coupling is only possible up to a critical thickness of the soft phase. Therefore, strong interphase exchange coupling is usually manifested only for nanostructured materials,[11] and the fabrication method and resulting micro- and nanostructure have strong impact on the final magnetic properties of hard/soft nanocomposites and multilayers.[12,13]

In crystalline heterostructures, the exchange coupling is often reduced at the interfaces due to structural transitions, defects, or both.[14–16] Multilayers and composites made using amorphous alloys have the advantage that undesirable effects from, for example, atomic steps at interfaces and other structural defects are avoided simply by the amorphous nature, resulting in smooth and continuous interfaces.[17,18] The alternative, to produce high quality epitaxial heterostructures of hard/soft magnets, is a much more cumbersome route toward smooth interfaces.[19] In addition, the epitaxial growth is limited to specific phases with matching lattice constants and specific magnetic properties. The magnetic properties of many amorphous building blocks can, on the other hand, be tuned almost continuously through their composition.[17,20] The sputter process allows industrial-scale production of amorphous multilayers with smooth interfaces, while recent advances in additive manufacturing of amorphous Fe-based materials open up new perspectives to create amorphous composite magnets of larger sizes and different shapes.[21,22]

In the present study, we combine amorphous magnetically hard $Sm_{15}Co_{85}$ and magnetically soft $Co_{85}(Al_{70}Zr_{30})_{15}$ layers in a series of samples with systematically varying design, from

P. Rani, Dr. G. Muscas,[+] Prof. G. Andersson, Dr. P. E. Jönsson
Department of Physics and Astronomy
Uppsala University
Box 35, SE-751 03, Uppsala, Sweden
E-mail: gabriella.andersson@physics.uu.se; petra.jonsson@physics.uu.se
Dr. H. Stopfel
Department of Materials Science and Engineering
Uppsala University
Box 534, SE-751 21, Uppsala, Sweden
The ORCID identification number(s) for the author(s) of this article can be found under https://doi.org/10.1002/aelm.202000573.
[+]Present address: Department of Physics, University of Cagliari, Monserrato I-09042, Italy

DOI: 10.1002/aelm.202000573

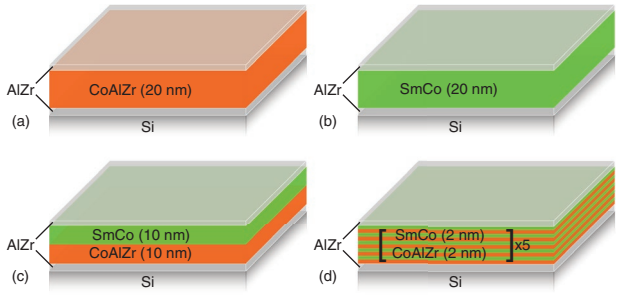

Figure 1. Schematic representation of the samples grown on Si substrates with $Al_{70}Zr_{30}$ (AlZr) as buffer and capping layers. The hard magnetic phase is $Sm_{15}Co_{85}$ (SmCo) shown in green and the soft magnetic phase is $Co_{85}(Al_{70}Zr_{30})_{15}$ (CoAlZr) shown in orange: a) a CoAlZr single layer sample, b) a SmCo single layer, c) a SmCo/CoAlZr bilayer sample, and d) a[SmCo/CoAlZr multilayer sample.

single films to multilayers. The aim is to investigate the interphase exchange coupling in a well-defined model system using both experimental techniques and micromagnetic simulations.

2. Results and Discussion

2.1. Structural Characterization

The samples under investigation consist of magnetically hard $Sm_{15}Co_{85}$ (SmCo) and soft $Co_{85}(Al_{70}Zr_{30})_{15}$ (CoAlZr) layers deposited by magnetron sputtering on Si substrates. The composites are in the form of a single bilayer SmCo(10 nm)/CoAlZr(10 nm), and a multilayer stack of [SmCo (2 nm)/CoAlZr (2 nm)]×5. The total thickness of the magnetic layers in each individual sample is 20 nm, and all samples including two reference magnetic single layer films are illustrated schematically in **Figure 1**. The sample structures started with a 4–5 nm $Al_{70}Zr_{30}$ buffer layer, to avoid the creation of crystallites in the magnetic layers.[17] A final protective cap layer of 4–5 nm $Al_{70}Zr_{30}$ prevents oxidation of the magnetic layers by the formation of a 2–3 nm thick self-passivating Al_2O_3 top layer upon exposure to air.

Grazing incidence X-ray diffraction (GIXRD) results from all samples are shown in **Figure 2**a. No Bragg peaks are observed for any of the samples; only broad features with a base width of at least 10° appear. This indicates that there is no crystalline precipitation, as expected for growth on the $Al_{70}Zr_{30}$ buffer layer,[17] and thus all the samples are X-ray amorphous. Figure 2b shows measured and fitted X-ray reflectivity (XRR) data. The individual layer thickness and interface roughness values of all samples, as obtained from fitting the XRR data with the *GenX* software,[23] are listed in **Table 1**. In all samples, narrow Kiessig fringes from the total thickness, and broader features from the capping layer, are clearly observable up to at least $2\theta \approx 5°$ which is an indication of well-defined layer thicknesses.

2.2. Magnetic Properties

All samples exhibited isotropic in-plane magnetization, except the CoAlZr single layer (as discussed in detail in Supporting Information). The CoAlZr sample shows uniaxial in-plane anisotropy that follows the alignment of the clips used for fixing the sample during the deposition.[24] This anisotropy is probably induced during the growth due to the strain of the substrate clamped to the sample holder in accordance with a recent study evidencing the appearance of uniaxial anisotropy in polycrystalline Co-films originating from strain during growth.[25]

The in-plane hysteresis loops of the samples, obtained by superconducting quantum interference device (SQUID) magnetometry measurements at room temperature, are shown in **Figure 3**. In the bilayer and multilayer samples, only one sharp switching can be seen suggesting that the CoAlZr and SmCo layers are strongly exchange coupled across the interfaces. All values of H_c, M_s, and remanent magnetization M_r are summarized in **Table 2**. The exchange-coupled layered samples have H_c and M_s values in-between those of the hard SmCo film and the soft CoAlZr film. We note, however, that the coercivity of amorphous SmCo films depends strongly, and in a non-monotonous way, on the film thickness for values below ≈30 nm.[26] The values of the coercivity obtained from the $M(H)$ loops can, therefore, not be taken as measures of the strength of the exchange coupling.

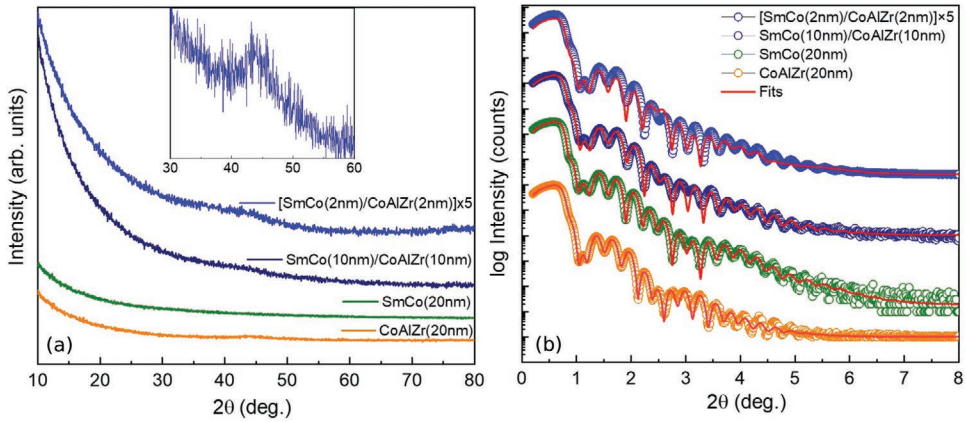

Figure 2. a) GIXRD measurements of (bottom to top) the CoAlZr (20 nm) single layer, the SmCo (20 nm) single layer, the SmCo (10 nm)/CoAlZr (10 nm) bilayer, and the [SmCo (2 nm)/CoAlZr (2 nm)]× 5 multilayer. Inset: an enlargement of the broad peak around $2\theta \approx 45°$ for the [SmCo (2 nm)/CoAlZr (2 nm)]× 5 multilayer. b) Measured XRR (points) and *GenX*[23] fits (lines). The parameters obtained by the *GenX* fits are presented in Table 1.

Table 1. Individual layer thickness t, and the corresponding interface roughness σ, of all layers in all samples, extracted from the *GenX* fits of the XRR data shown in Figure 2.

Layer	SmCo (20 nm)		CoAlZr (20 nm)		SmCo (10 nm)/CoAlZr (10 nm)		[SmCo (2nm)/CoAlZr (2nm)] × 5	
	t [nm] ± 0.5	σ [nm] ± 0.5	t [nm] ± 0.5	σ [nm] ± 0.5	t [nm] ± 0.5	σ [nm] ± 0.5	t [nm] ± 0.5	σ [nm] ± 0.5
Al_2O_3	2.3	0.8	2.2	0.9	2.0	0.9	2.5	1.0
$Al_{70}Zr_{30}$ capping	3.5	0.7	3.6	0.6	3.6	0.5	3.4	0.7
$Sm_{15}Co_{85}$	21.3	1.0	–	–	10.0	0.9	2.0	0.8
$Co_{85}(Al_{70}Zr_{30})_{15}$	–	–	20.0	1.1	10.0	1.0	2.0	1.1
$Al_{70}Zr_{30}$ buffer	4.6	1.0	4.3	0.6	4.2	0.9	4.3	0.8
SiO_2	2.5	0.5	4.3	0.9	2.3	0.4	3.1	0.4

The number densities of CoAlZr and SmCo are first estimated, from the fits of the individual films, to be 86 and 71 nm^{-3}, respectively. Later, these values are fixed for all samples to obtain each individual layer thickness and the corresponding roughness. To capture the effect of the partial oxidation of the AlZr capping layer, we added an additional Al_2O_3 layer on top of the capping layer. The SiO_2 layer is the natural oxide layer on top of the Si substrate. To reduce the number of free parameters, the densities of the Al_2O_3 and the SiO_2 layers have been fixed to standard values.

The first-order reversal curve (FORC) technique is the only experimental method that provides detailed information about the switching field distribution, and thereby the internal coupling phenomena. FORCs were recorded at room temperature starting at positive saturation of the magnetic sample, and then the applied field was ramped down to a reversal field H_r. The magnetization $M(H, H_r)$ is measured as the applied field H is increased back toward positive saturation. The process is repeated with successively decreasing reversal fields. During a conventional $M(H)$ loop, the continuous sweeping of the field from one saturation value to the opposite induces a reversal process where all internal reversal events are influenced simultaneously by both the applied field and the internal interactions. On the other hand, scanning reversal fields according to the FORC protocol allows to deconvolute the effects of the applied field and the internal interactions.

The FORC distribution, $\rho(H, H_r)$, is defined as the mixed second derivative of $M(H, H_r)$

$$\rho(H,H_r) = -\frac{1}{2M_s}\frac{\partial^2 M(H,H_r)}{\partial H\,\partial H_r} \quad (1)$$

and was calculated using the FORCinel algorithm[27] implemented in a Matlab code. **Figure 4** shows the contour plots of the FORC distribution function ρ versus H and H_r for all samples. The magnetization reversal of CoAlZr is characterized by a single sharp positive signal (Figure 4a), indicating a sharp and narrow distribution of switching fields. The single layer SmCo sample, on the other hand, exhibits two positive peaks and a large negative signal in the FORC diagram (Figure 4b). This is typical for magnetic materials with a quite broad distribution of switching fields and strong internal interactions.[18,28] We note that the single-phase amorphous materials are not homogeneous below the length scale of about 10 nm[29] and that the high resolution of the FORC protocol allows us to evidence the presence of two sub-populations of regions with slightly different coercivity. For both the SmCo/CoAlZr bilayer and multilayer samples (Figure 4c,d), only one single positive signal is observed, similar to the CoAlZr sample. Hence, the FORCs provide direct evidence of strong exchange coupling in these samples. Moreover, the switching field distribution further narrows down in the multilayer compared to the bilayer, indicating that the exchange coupling is even stronger in the multilayer.[30] It is interesting that the distribution of switching fields is narrower in the hard/soft layered samples than for the single layer SmCo sample, since it indicates that the effect of the soft phase in the amorphous nanocomposites is not only to reduce the amount of rare-earth material and to increase the overall saturation magnetization, but also to narrow down the switching field distribution.

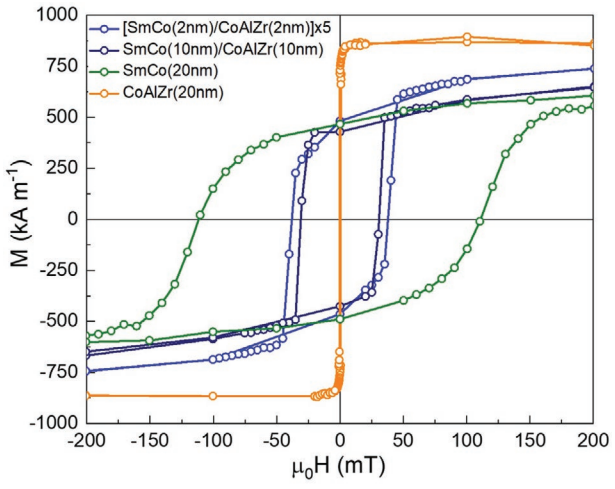

Figure 3. In-plane SQUID hysteresis loops at room temperature of all four samples. The diamagnetic signal from the Si substrate has been subtracted.

2.3. Micromagnetic Simulations

Micromagnetic simulations, employing a model with continuous amorphous interfaces, were used to study in detail the exchange coupling between SmCo and CoAlZr and to find the critical thickness for exchange coupling. To reproduce the magnetic structure of the amorphous alloys, a random anisotropy model (RAM) was implemented,[31,32] assigning to each cell a randomly oriented easy axis direction. The local

Table 2. Coercivity $\mu_0 H_c$, remanent magnetization M_r, and saturation magnetization M_s obtained from SQUID measurements of $M(H)$ at room temperature.

Sample	$\mu_0 H_c$ [mT]	M_r [kA m^{-1}]	M_s [kA m^{-1}]
CoAlZr (20 nm)	0.40 (1)	740 (10)	866 (6)
SmCo (20 nm)	111 (1)	485 (1)	716 (2)
SmCo (10 nm)/CoAlZr (10 nm)	30 (3)	426 (8)	741 (3)
[SmCo (2 nm)/CoAlZr (2 nm)] × 5	39 (3)	454 (10)	770 (4)

The CoAlZr sample was measured along the side of the sample close to the easy axis. The other samples exhibit isotropic in-plane magnetization.

anisotropy magnitudes in the cells were adjusted to reproduce the experimental $M(H)$ curves of the individual CoAlZr and SmCo phases. The multilayer structures have been simulated using the same parameters as for the individual phases. The experimental $M(H)$ loops are reproduced (as shown in Supporting Information) without taking into account any reduction of exchange coupling at the interfaces. Reduced exchange interactions at the interfaces is a phenomenon that often occurs in conventional crystalline heterostructures due to structural transitions between the magnetic phases, interface disorder, and roughness.[15] The success of the continuous amorphous interface model in reproducing the experimental data, without reducing the exchange coupling at the interfaces, emphasizes the advantage of all-amorphous multilayers, where the absence of sharp structural interfaces preserves the exchange coupling over longer length scales compared to crystalline magnetic composite structures.[18]

According to the Goto model for interfacial exchange-spring coupling between a soft and a hard phase, the two phases can reverse their moment coherently, that is, as a single component, only if the coupling is strong enough to extend from the interface throughout the full thickness of the soft phase.[10] The maximum thickness of the soft phase through which the rigid coupling can extend is called the critical thickness

$$t_s^{\text{crit}} = \sqrt{\frac{\pi^2 A_{\text{soft}}}{2M_s^{\text{soft}} \mu_0 H_r^{\text{hard}}}} \tag{2}$$

Here, A_{soft} and M_s^{soft} are the exchange stiffness and saturation magnetization of the soft phase, respectively, and H_r^{hard} is the reversal field of the hard phase. Considering $A_{\text{soft}} = 12$ pJ/m, the critical thickness for the investigated materials has been estimated to be ≈25 nm, which is well above the thickness of the soft layer in both composite samples. This is consistent with the experimental observation of a single-phase behavior, that is, coherent switching, in both the [SmCo (2 nm)/CoAlZr (2 nm)]×5 and the SmCo (10 nm)/CoAlZr (10 nm) samples.

Additional micromagnetic simulations have been performed to investigate the limit of the rigid exchange coupling. Maintaining the 1:1 proportion of the two phases, we have simulated virtual samples with increasing thickness of both phases of 20, 30, and 50 nm. **Figure 5**a shows the $M(H)$ curves obtained from simulations of [SmCo (2 nm)/CoAlZr (2 nm)]×5, SmCo (10 nm)/CoAlZr (10 nm), and SmCo (50 nm)/CoAlZr (50 nm). The first two samples show a sharp single-phase reversal, as seen in the illustration of the typical spin reversal process presented in Figures 5b,c, with both the hard and the soft phase

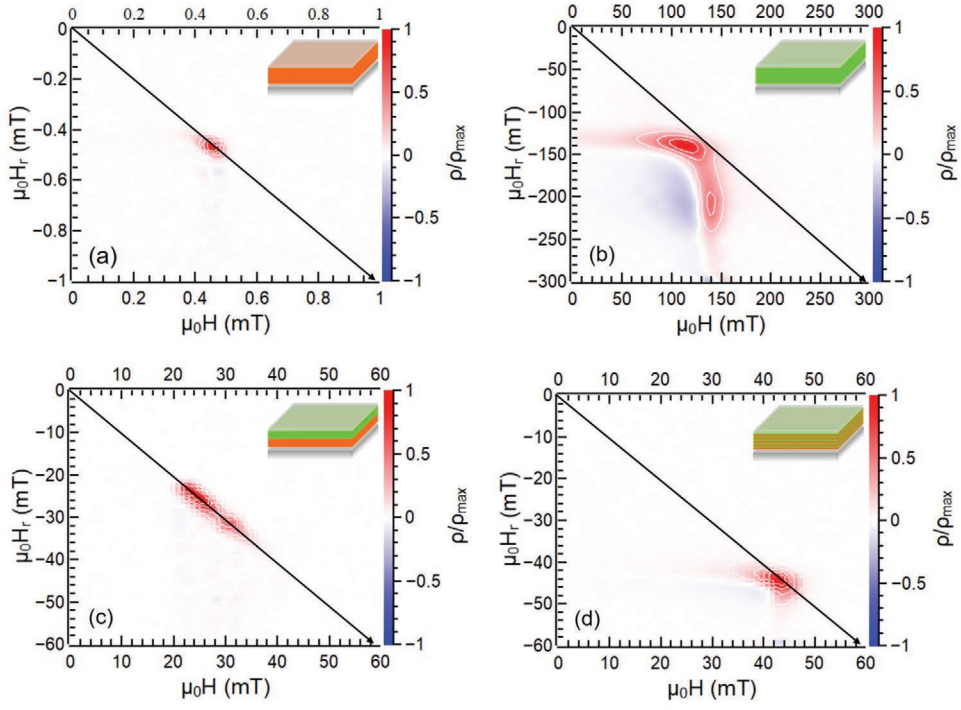

Figure 4. Room temperature FORC diagrams for a) CoAlZr (20nm), b) SmCo (20nm), c) SmCo (10nm)/CoAlZr (10nm), d) [(SmCo (2nm)/CoAlZr (2nm)]×5. The color bar indicates the normalized value of ρ in the FORC. The FORC measurements were performed in the L-MOKE setup only for the CoAlZr (20nm) sample, and in the VSM for the other samples.

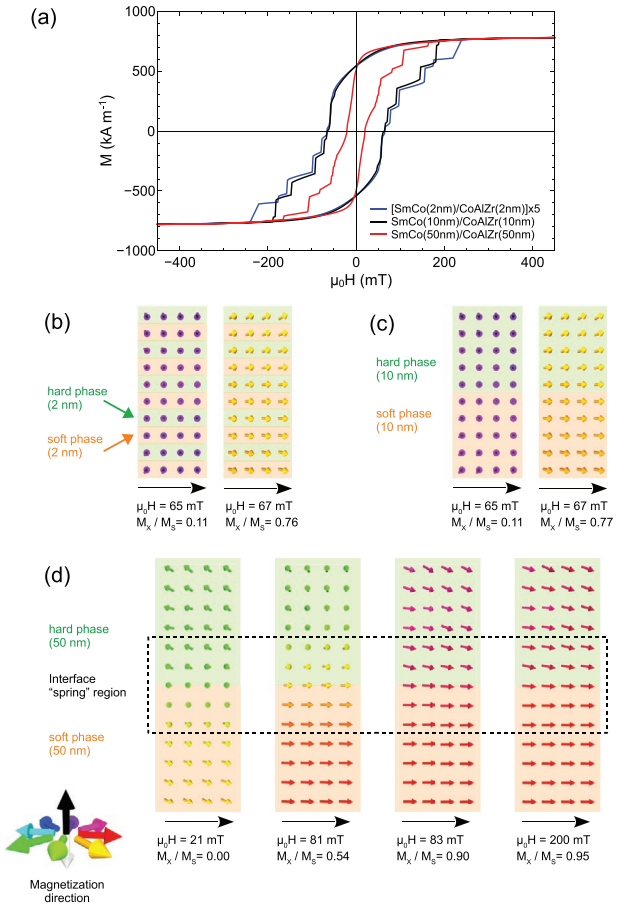

Figure 5. a) Magnetization versus field curves obtained from micromagnetic simulations for [SmCo (2 nm)/CoAlZr (2 nm)]×5 (blue curve), SmCo (10 nm)/CoAlZr (10 nm) (black curve), and the virtual sample SmCo (50 nm)/CoAlZr (50 nm) (red curve). Each curve is an average over ten simulations with different random configurations. b–d) Vertical cross sections illustrating the typical switching in one simulation of b) [SmCo (2 nm)/CoAlZr (2 nm)]×5, c) SmCo (10 nm)/CoAlZr (10 nm), and d) SmCo (50 nm)/CoAlZr (50 nm). The arrows represent the magnetization vector within an individual cell in (b) and (c), and the average magnetization over about 4 cells in (d).

switching simultaneously within a narrow field range. In agreement with the estimated critical thickness of 25 nm, Figure 5d reveals a two-step spin reversal process for SmCo(50 nm)/CoAlZr(50 nm), initiated by the soft phase in which only a limited interface region pins to the hard phase. The exchange-spring behavior in the interface region results in a lower coercivity in the $M(H)$ curve (Figure 5a) for the sample with 50 nm layer thickness compared to those with 10 nm and 2 nm.

3. Conclusion

We have shown that strong exchange coupling is possible between two amorphous phases, using an amorphous hard/soft multilayer model system. The tunability of the magnetic properties of amorphous magnets with the chemical composition could be used to further improve the magnetic properties of the soft phase. For a high saturation magnetization of the amorphous soft phase, the best choice would be $(Fe_{1-x}Co_x)$ – A, with $x \approx 0.3$ and A being one or several glass formers at the lowest glass-forming concentration.[33,34] To obtain a large critical thickness of the soft phase, a high exchange stiffness A_{soft} is preferred according to Equation (2). For crystalline Co-X, several non-magnetic dopants have been shown to decrease not only the saturation magnetization but also the exchange stiffness. Doping with Fe, on the other hand, results in an increase of the saturation magnetization while the exchange stiffness is unaffected.[35] It would be interesting to investigate how different glass formers affect the exchange stiffness for amorphous $(Fe_{1-x}Co_x)$ – A. The method to extract the exchange stiffness based on the spin spiral formation in two ferromagnetic films antiferromagnetically coupled across a non-magnetic spacer layer, is in addition suitable for investigating its thickness dependence.[35,36] The coercivity of the hard phase, that is, the SmCo magnet, can also be tuned by the composition.[17]

Geometrical factors can also be used to improve the properties of hard/soft nanocomposites.[13,37] However, all possible methods to improve the magnetic properties of two-phase magnets require a strong exchange coupling between them. We have shown here that the exchange coupling between two amorphous phases can easily be rigid. The magnetization reversal process investigated by FORC clearly shows the improvement obtained by coupling the soft/hard amorphous phases in multilayers with thin individual layers. Micromagnetic simulations have successfully been used to reproduce the experimental data with a continuous interface model, that is, simulating an ideal, fully amorphous, structure without any structural discontinuity. This allows us to conclude that the strategy of using amorphous nanocomposites to obtain rigid exchange coupling between a hard and a soft magnetic phase provides undeniable advantages compared to conventional crystalline composites; offering, at the same time, additional degrees of freedom to improve and finely tune the magnetic properties. Recent advances in additive manufacturing of amorphous Fe-based materials open up new perspectives to create amorphous composite magnets of various sizes and shapes and with controlled microstructure.[21,22]

4. Experimental Section

Sample Preparation: Samples were prepared by DC magnetron co-sputtering of Sm, Co, and $Al_{70}Zr_{30}$ targets, onto Si (100) substrates, in an ultra-high vacuum chamber with a base pressure below $\approx 10^{-9}$ Torr. The sputtering gas was Ar of 99.99% purity and the pressure was 2.0×10^{-3} Torr. The substrates were annealed in vacuum at 300 °C for 30 min to remove water vapor and surface impurities. After cooling to room temperature, the sample holder was rotated at 20 rpm for a homogeneous growth with respect to both thickness and composition.

Characterization Techniques: In order to examine the structural quality of the samples, grazing incidence X-ray diffraction (GIXRD) and X-ray reflectivity (XRR) measurements on 1×1 cm^2 square sample pieces were performed. The GIXRD and XRR patterns were collected using a Bruker D8 Da Vinci diffractometer, in a standard Bragg–Brentano geometry, operating at 40 kV and 30 mA with CuK_α ($\lambda = 1.54$Å) radiation. The GIXRD scans were performed in continuous scan mode with the scattering angle in the range 2θ = 10 to 80°, 0.05° step size, and a grazing incident angle of 1°.

A superconducting quantum interference device (SQUID) magnetometer (Quantum Design MPMS 5 XL) was used to measure

both room- and low-temperature magnetization versus field, $M(H)$, curves for all samples. First-order reversal curves (FORC), were recorded at room temperature using a vibrating sample magnetometer (VSM; Lake Shore VSM model 7400) operated in a field range of ±1 T, and a field sweeping rate of 10–50 mT min^{-1}. Due to its ultra-soft character, the FORCs of the CoAlZr sample were instead recorded with a longitudinal magneto-optical Kerr effect (L-MOKE) setup, operating at higher resolution in a field range of ±20 mT, with a sweeping rate of 20 mT s^{-1}. The L-MOKE setup was equipped with a red laser (wavelength 660 nm) modulated by a wave generator at 13 kHz and the light intensity was measured using a biased Si photodetector coupled to a lock-in amplifier (SR830). To improve the signal-to-noise ratio, each FORC curve was the average of five individual loops measured in sequence.

Micromagnetic simulations were performed using MuMax^3, a GPU-accelerated micromagnetic simulation software that employs a finite difference discretization of space.[38] The room temperature $M(H)$ curves were simulated using the experimental saturation magnetization (M_s) values of the CoAlZr and SmCo phases, and the same exchange stiffness constant $A_{ex} = 12$ pJ m^{-1} for both; this being a typical room temperature value for amorphous alloys with Co content above 80 at%.[39–41] The system was meshed into unit cells of $2 \times 2 \times 2$ nm^3, that is, smaller than the calculated exchange length ($L_{ex} = \sqrt{2A_{ex}/\mu_0 M_s^2}$) for the pure soft and hard phases, which are approximately 5 nm and 6 nm, respectively. A random anisotropy model (RAM) was implemented,[31,32] assigning to each cell a randomly oriented easy axis direction, with the magnetic anisotropy constant values following a Gaussian distribution with average values of 8 kJ m^{-3} and 1.75 MJ m^{-3} for CoAlZr and SmCo, respectively, with 20% standard deviation in both cases. These values were obtained by optimizing the reproduction of the experimental $M(H)$ loops, as discussed in Supporting Information. Periodic boundary conditions were applied in the x and y directions, and the systems were simulated using 64×64 cells. In the z direction, the number of cells depended on the total thickness of the magnetic sample. For each system, the simulations were averaged over ten different starting seeds, to account for different local random structures produced by the pseudo-random generator of the micromagnetic simulation code.

Supporting Information

Supporting Information is available from the Wiley Online Library or from the author.

Acknowledgements

P.R. and G.M. contributed equally to this work. The work presented here was conducted with financial support from the Swedish Research Council (Contract Number 2017-03725) and the Carl-Tryggers Foundation, which is gratefully acknowledged.

Conflict of Interest

The authors declare no conflict of interest.

Keywords

exchange coupling, exchange-spring magnets, first-order reversal curve technique, magnetron sputtering, micromagnetic simulations, nanocomposites, nanomagnetism

Received: June 3, 2020
Revised: September 13, 2020
Published online:

[1] R. Skomski, P. Manchanda, P. Kumar, B. Balamurugan, A. Kashyap, D. Sellmyer, *IEEE Trans. Magn.* **2013**, *49*, 3215.
[2] A. Nayak, M. Nicklas, S. Chadov, P. Khuntia, C. Shekhar, A. Kalache, M. Baenitz, Y. Skourski, V. Guduru, A. Puri, U. Zeitler, J. Coey, C. Felser, *Nat. Mater.* **2015**, *14*, 679.
[3] K. Smith Stegen, *Energy Policy* **2015**, *79*, 1.
[4] R. Skomski, J. Coey, *Scr. Mater.* **2016**, *112*, 3.
[5] N. Poudyal, J. P. Liu, *J. Phys. D: Appl. Phys.* **2013**, *46*, 043001.
[6] E. F. Kneller, R. Hawig, *IEEE Trans. Magn.* **1991**, *27*, 3588.
[7] R. Skomski, J. M. D. Coey, *Phys. Rev. B* **1993**, *48*, 15812.
[8] J. Coey, *IEEE Trans. Magn.* **2011**, *47*, 4671.
[9] F. Liu, Y. Hou, S. Gao, *Chem. Soc. Rev.* **2014**, *43*, 8098.
[10] E. Goto, N. Hayashi, T. Miyashita, K. Nakagawa, *J. Appl. Phys.* **1965**, *36*, 2951.
[11] A. Lopez-Ortega, M. Estrader, G. Salazar-Alvarez, A. G. Roca, J. Nogues, *Phys. Rep.* **2015**, *553*, 1.
[12] O. Gutfleisch, *J. Phys. D. Appl. Phys.* **2000**, *33*, R157.
[13] J. S. Jiang, S. D. Bader, *J. Phys. Condens. Matter* **2014**, *26*, 064214.
[14] W. Si, G. P. Zhao, N. Ran, Y. Peng, F. J. Morvan, X. L. Wan, *Sci. Rep.* **2015**, *5*, 16212.
[15] S. Sabet, A. Moradabadi, S. Gorji, M. Yi, Q. Gong, M. Fawey, E. Hildebrandt, D. Wang, H. Zhang, B.-X. Xu, C. Kübel, L. Alff, *Phys. Rev. B* **2018**, *98*, 174440.
[16] Y. Deng, G. Zhao, L. Chen, H. Zhang, X. Zhou, *J. Magn. Magn. Mater.* **2011**, *323*, 535.
[17] F. Magnus, R. Moubah, A. H. Roos, A. Kruk, V. Kapaklis, T. Hase, B. Hjörvarsson, G. Andersson, *Appl. Phys. Lett.* **2013**, *102*, 162402.
[18] G. Muscas, R. Brucas, P. E. Jönsson, *Phys. Rev. B* **2018**, *97*, 174409.
[19] S. Sabet, A. Moradabadi, S. Gorji, M. Fawey, E. Hildebrandt, I. Radulov, D. Wang, H. Zhang, C. Kübel, L. Alff, *Phys. Rev. Appl.* **2019**, *11*, 054078.
[20] S. Yamamoto, M. Taguchi, T. Someya, Y. Kubota, S. Ito, H. Wadati, M. Fujisawa, F. Capotondi, E. Pedersoli, M. Manfredda, L. Raimondi, M. Kiskinova, J. Fujii, P. Moras, T. Tsuyama, T. Nakamura, T. Kato, T. Higashide, S. Iwata, S. Yamamoto, S. Shin, I. Matsuda, *Rev. Sci. Instrum.* **2015**, *86*, 083901.
[21] Z. Mahbooba, L. Thorsson, M. Unosson, P. Skoglund, H. West, T. Horn, C. Rock, E. Vogli, O. Harrysson, *Appl. Mater. Today* **2018**, *11*, 264.
[22] N. Luo, C. Scheitler, N. Ciftci, F. Galgon, Z. Fu, V. Uhlenwinkel, M. Schmidt, C. Körner, *Mater. Charact.* **2020**, *162*, 110206.
[23] M. Björck, G. Andersson, *J. Appl. Crystallogr.* **2007**, *40*, 1174.
[24] A. Frisk, *Ph.D. Thesis*, Acta Universitatis Upsaliensis, **2016**.
[25] A. S. Dev, D. Kumar, P. Gupta, P. Vishwakarma, A. Gupta, *Mater. Res. Bull.* **2020**, *121*, 110616.
[26] R. Moubah, F. Magnus, E. Östman, Y. Muhammad, U. B. Arnalds, M. Ahlberg, B. Hjörvarsson, G. Andersson, *J. Phys. Condens. Matter* **2013**, *25*, 416004.
[27] R. J. Harrison, J. M. Feinberg, presented at AGU Fall Meeting, San Francisco, CA **2007**.
[28] D. A. Gilbert, G. T. Zimanyi, R. K. Dumas, M. Winklhofer, A. Gomez, N. Eibagi, J. Vicent, K. Liu, *Sci. Rep.* **2014**, *4*, 4204.
[29] R. Gemma, M. to Baben, A. Pundt, V. Kapaklis, B. Hjörvarsson, *Sci. Rep.* **2020**, *10*, 11410.
[30] K. Pandey, J. Chen, G. Chow, *IEEE Trans. Magn.* **2010**, *46*, 1955.
[31] R. Alben, J. Becker, M. Chi, *J. Appl. Phys.* **1978**, *49*, 1653.
[32] G. Herzer, *Properties and Applications of Nanocrystalline Alloys from Amorphous Precursors*, NATO Science Series (Eds: B. Idzikowski, P. Švec, M. Miglierini), Vol. *184*, Kluwer Academic Publishers, Dordrecht, The Netherlands **2005**, pp. 15–34.
[33] P. V. Paluskar, R. Lavrijsen, M. Sicot, J. T. Kohlhepp, H. J. M. Swagten, B. Koopmans, *Phys. Rev. Lett.* **2009**, *102*, 016602.
[34] A. Frisk, M. Ahlberg, G. Muscas, S. George, R. Johansson, W. Klysubun, P. E. Jönsson, G. Andersson, *Phys. Rev. Materials* **2019**, *3*, 074403.

[35] C. Eyrich, A. Zamani, W. Huttema, M. Arora, D. Harrison, F. Rashidi, D. Broun, B. Heinrich, O. Mryasov, M. Ahlberg, O. Karis, P. E. Jönsson, M. From, X. Zhu, E. Girt, *Phys. Rev. B* **2014**, *90*, 235408.
[36] E. Girt, W. Huttema, O. N. Mryasov, E. Montoya, B. Kardasz, C. Eyrich, B. Heinrich, A. Y. Dobin, O. Karis, *J. Appl. Phys.* **2011**, *109*, 07B765.
[37] R. Skomski, G. C. Hadjipanayis, D. J. Sellmyer, *J. Appl. Phys.* **2009**, *105*, 07A733.
[38] A. Vansteenkiste, J. Leliaert, M. Dvornik, M. Helsen, F. Garcia-Sanchez, B. Van Waeyenberge, *AIP Adv.* **2014**, *4*, 107133.
[39] S. C. Yu, W. Y. Lim, J. S. Baek, Y. Y. Kim, K. W. Rhie, S. H. Lee, *J. Appl. Phys.* **2002**, *85*, 6004.
[40] P. Spisak, M. Konc, T. Reininger, P. Kollar, P. Sovak, O. Dusa, *IEEE Trans. Magn.* **2002**, *30*, 524.
[41] G. Buttino, A. Cecchetti, M. Poppi, *J. Magn. Magn. Mater.* **1997**, *172*, 147.